Active Cooling Substrates for Thermal Management of Microelectronics

Yong Wang, Guang Yuan, Yong-Kyu Yoon, *Student Member, IEEE*, Mark G. Allen, *Member, IEEE*, and Sue Ann Bidstrup

***Abstract*—Heat removal in printed wiring boards (PWB) is primarily accomplished through conduction. This work presents a microelectromechanical system (MEMS) device comprised of an active cooling substrate (ACS) designed and fabricated to add fluidic cooling functionality to the PWB. Thermal management is enhanced through the additional heat convection mode. Synthetic jet technology makes the compact, but easily integrated, MEMS cooling device possible. The fluid control unit, a synthetic jet, has been implemented in an epoxy-glass printed wiring board by multilayer lamination. An air reservoir is drilled through the core of printed wiring board. A flexible polymeric diaphragm and a low profile electromagnetic driver create an active pumping system to produce vibrating air jets downstream of microfluidic channels which transports heat generated by hot microelectronic components. Test heater chips have been directly die attached to the substrate. The integrated packaging system has been characterized mechanically, electrically, and thermally. Peak jet velocities of 14 m/s and average jet velocities of approximately 3 m/s have been achieved at actuator powers of 60 mW. This integrated active cooling substrate has the potential for broad applications in thermal management at the system packaging level.**

***Index Terms*—Active cooling substrate, electromagnetic actuator, printed wiring board (PWB), synthetic jet, thermal management.**

I. Introduction

THERMAL management is a challenging issue in microsystems packaging. Increased power consumption of advanced microsystem devices coupled with increasingly compact packages result in increased demands on thermal management. For example, the transistors on lead Intel microprocessors double every two years, the die size grows by 14% every two years, and the frequency doubles every two years. In terms of power consumption, the past 486 processor is about 2 W, the current Pentium processor is about 100 W, and the future processor in the year of 2008 is expected to be 10 000 W [1].

Manuscript received August 25, 2003; revised August 4, 2004. This work was supported in part by the Defense Advanced Research Projects Agency (DARPA) under its Heat Removal Using Thermo-Integrated Circuits (HERETIC) Program and Dyneon LLC. This work was recommended for publication by Associate Editor T. Lee upon evaluation of the reviewers' comments.

Y. Wang and S. A. Bidstrup are with the School of Chemical and Biomolecular Engineering, Georgia Institute of Technology, Atlanta, GA 30332-0100 USA (e-mail: sue.bidstrup@chbe.gatech.edu).

G. Yuan and Y.-K. Yoon are with the School of Electrical and Computer Engineering, Georgia Institute of Technology, Atlanta, GA 30332-0250 USA.

M. G. Allen is with the School of Electrical and Computer Engineering, Georgia Institute of Technology, Atlanta, GA 30332-0250 USA and also with the School of Chemical and Biomolecular Engineering, Georgia Institute of Technology, Atlanta, GA 30332-0100 USA.

Digital Object Identifier 10.1109/TCAPT.2005.848575

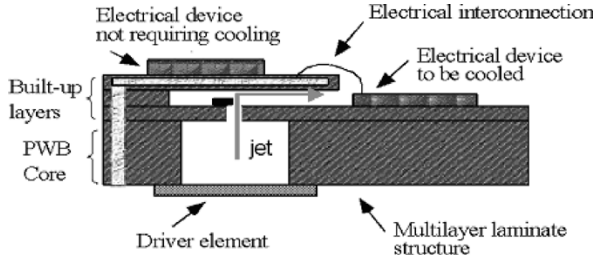

Fig. 1. Schematic of the active cooling substrate.

Fans coupled with heat sinks are the traditional approach to realize system-level global heat convection. The fan efficiency is defined as the ratio of the useful power output to the power input. The efficiency of these fans is low, i.e., backward curved fans have efficiencies about 80% [2]. Another challenge in thermal management is nonuniformity of the power distribution. Heat spreaders and thermal vias are used in the package to enhance local heat conduction [3]. Printed-wiring-board microfluidics are a promising microelectromechanical system (MEMS) solution to this problem by enhancing the local heat convection. Printed wiring boards (PWB's) are a composite of organic (i.e., epoxy) and inorganic (i.e., glass fiber) materials with external and internal wiring, allowing electronic components to be mechanically supported and electrically connected. One of the goals of this study is to also incorporate fluidic channels into the PWB. This would result in an increase in the functionality of the PWB to include thermal management as well as electrical interconnection and mechanical support. Fig. 1 shows the concept of an active cooling substrate (ACS) with fluidic functionality built in the PWB substrate. A heat carrier fluid, either in liquid state or in gas state, is driven through the fluidic passages and removes the heat generated by the thermally active electronic devices.

To achieve this goal, two requirements must be met. A low ACS profile and compatibility with the PWB manufacturing process. PWB are typically around 2 mm in thickness. The use of synthetic jets is an attractive approach to realize low profile due to the simple structures [4], [5]. Fig. 2 illustrates the concept of the synthetic jet driver. A jet cavity is bounded on one side by a rigid plate bearing an orifice hole and on the other side by a flexible diaphragm. The vibration of the membrane results in the alternating entrainment and expulsion of air into and out of the cavity through the orifice hole.

Compared with fans, this MEMS approach can be easily combined with a single chip packaging (SCP) or a multichip packaging (MCP) and generates a synthetic jet locally at the

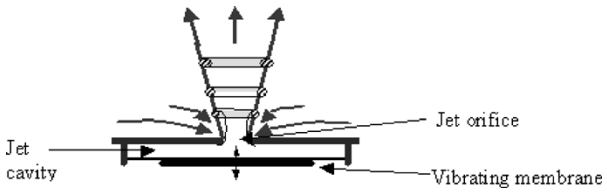

Fig. 2. Schematic of a synthetic jet.

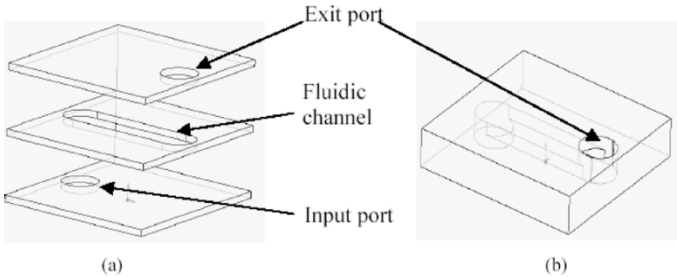

Fig. 3. Lamination process for fluidic structure (a) patterned multilayers and (b) laminated PWB.

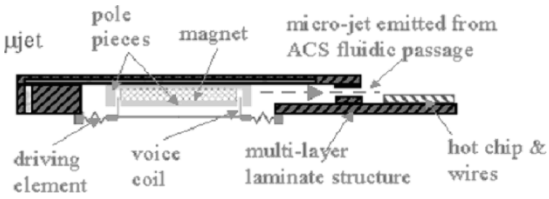

Fig. 4. Active cooling substrate with electromagnetic driver.

heat-emitting component to eliminate hot spots. The jet has low power requirements and a high thermal management efficiency which is realized by pinpoint cooling. In this research work, a synthetic-jet-based microfluidic structure is designed and fabricated. The fluid mechanics and cooling performance of the device are investigated.

II. Device Concept

As shown in Fig. 1, the synthetic jet is fabricated by drilling a large hole in the PWB core to form the jet cavity. The driver is embedded into the jet cavity, and the fluidic passages can be fabricated in the PWB built-up layers. Fig. 3 shows the basic steps of the lamination process for the formation of integrated fluidic channels. Multiple layers of prepreg laminates are patterned either by mechanical drilling or laser cutting to form the fluidic channels. Other microvia generation technologies i.e., plasma, reactive ion etching, and photolithography are also applicable to fabricate the fluidic channels. All of the functional layers are stacked, aligned, and laminated to form the microjet structure. Lamination is performed in a hot press tool. High temperature and forces are applied to the stacked laminates, and the epoxy adhesives are cured to bond the multiplayer structure together. This entire process is compatible with traditional PWB process.

The schematic of the designed MEMS device is shown in Fig. 4. It includes a driver which generates synthetic jet, a fluidic passage which helps to vector and position the jet and a heater array which mimics the heat generating components of an integrated circuitry. No externally supplied flow or complex pumping and pipeline system is required which simplifies the design and fabrication of the active cooling substrate.

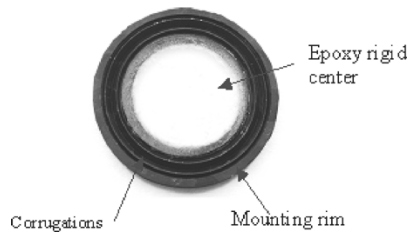

Fig. 5. Structure of diaphragm design.

The jet actuator is the core of the system module. An electromagnetic actuator is used to drive the synthetic jet. There are three important components to the actuator: a flexible, elastic diaphragm; a coil mounted on the flexible diaphragm, which can be driven using an alternating current (ac); and a permanent magnet which offers a constant magnetic field. The latter two parts form the driving circuit to vibrate the diaphragm.

The diaphragm material must be flexible, with a low Young's modulus, enabling a large displacement with a small applied force. In addition, to increase the efficiency of the device, air leakage must be prevented. Thus, the diaphragm is laminated on the printed wiring board (PWB) to ensure tight contact. The polymer selected must also be able to survive the PWB lamination process. In this study, a Dyneon fluoroelastomer (a compound of 75% Dyneon FE-5621Q and 25% FC-2145 by weight) was chosen as the diaphragm material. This material has good mechanical properties, with tensile modulus of 1.46 MPa at 100% elongation. It also has the advantage of both being able to survive the lamination process as well as being able to be molded into a variety of shapes. In order to achieve large displacements for a given force, concentric circular corrugations are molded into the polymeric diaphragm. The corrugation structure can increase the linear deflection range of the diaphragm [6]. The central region where the electromagnetic force is applied on the diaphragm must be rigid enough not to appreciably bend under load, and large enough in diameter to prevent bulging of the unsupported area of the diaphragm. Low-density material epoxy prepreg is selected to build a rigid center instead of the elastomer because it is much stiffer material than the Dyneon elastomer. Therefore, less material is required to make the rigid center, dramatically reducing the total mass of the diaphragm as well as the force necessary to drive it. The structure of the corrugated diaphragm is shown in Fig. 5.

The diaphragm design is directly related to the jet final cooling performance. The diaphragm structure determines the optimal vibration frequency and magnitude, both of which have significant impact on the synthetic jets volumetric flow rate. From the energy cost perspective, it is desirable to obtain maximum diaphragm displacement with a smaller driving force, namely a smaller coil driving current. Increasing the volumetric flow rate has two effects; first a greater jet flow will carry away more heat; second, a more powerful jet flow will entrain additional airflow, which also removes more heat. Design details are published elsewhere [7], [8]. A mechanical simulation package, ANSYS (by ANSYS Inc.), is also used to

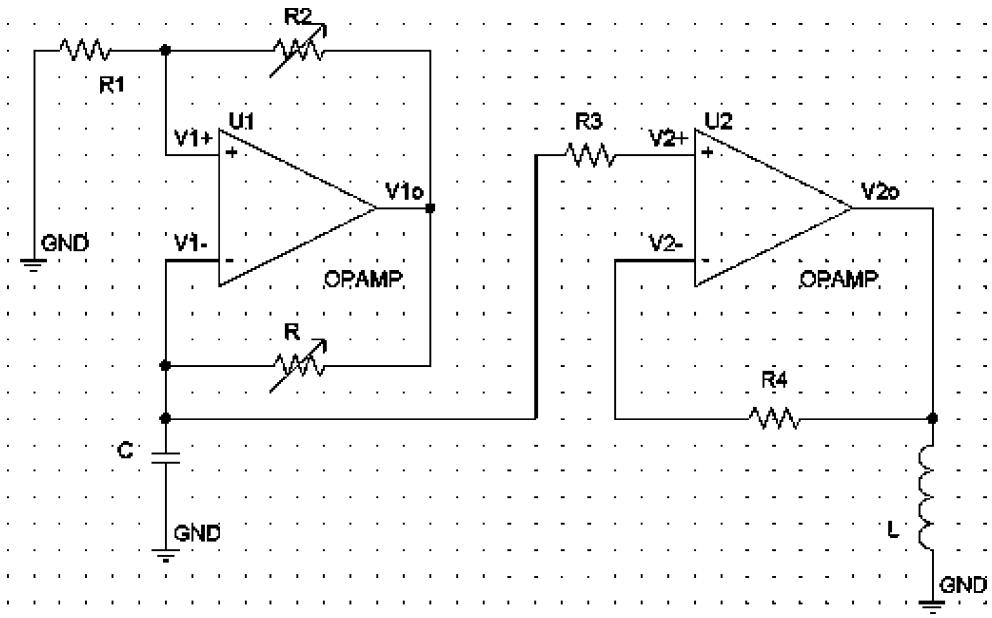

Fig. 6. Stable multivibrator driving circuit schematic.

model the deflection under an applied force to crosscheck the design results.

An optimized diaphragm structure is shown in Fig. 5. This diaphragm has a diameter of 33 mm. Epoxy prepreg is cut into circular sheet 24 mm in diameter and glued at the opened center of the diaphragm surrounded by elastomer corrugation structures. The diaphragm has one and a half 60° triangular corrugation structures, 2.2 mm in depth and 0.2 mm in thickness. This diaphragm has a resonant frequency of approximately 100 Hz.

The diaphragm vibration is excited by electromagnetic force. The driving circuitry includes a self-supporting air coil and a permanent magnet as shown in Fig. 4. The coil is wound by using 0.08-mm diameter copper wire with a 21-mm inner diameter and is 3 mm in height. The coil has an electrical resistance of approximately 12 ohms. It is glued on the diaphragm rigid center by using cyanoacrylate superglue. A 20-mm diameter Sm-Co magnet is placed in the center of the permalloy back iron. The back iron is glued to the center of substrate cavity, which has a circular recess 22 mm in diameter and 4 mm in depth to hold the magnet. A permalloy lid covers the magnet and completes the magnetic circuit. The magnet and the coil are aligned so that the coil can be driven to move in the gap between the magnet and the back iron upon application of ac current to the coil.

An ac current is generated by an astable multivibrator circuit as shown in Fig. 6 [9]. This circuit consists of two active components-two op amps (U1, U2), six passive components-three resistors (R1, R3, R4), two potentiometers (R, R2) and one capacitor (C). L is the coil loaded at the output. The first op amp U1 and R1, R2 form a bistable multivibrator. When V1o is positively saturated at $V_{sat}+$, V1+ will keep constant at $(V_{sat}+)R1/(R1+R2)$, the capacitor will be charged through R, so V1− increases exponentially; when V1o is negatively saturated, the capacitor will be discharged so V1− decreased exponentially. The second op amp U2 is the output stage which works as a buffer amplifier to drive the load. Two resistors R3, R4 help to reduce signal distortion when op amps are not so ideal. This circuit has no stable states and thus is named an astable multivibrator. Period T of this circuit is defined by (1)

$$T = 2RC \ln \left[\frac{1 + \frac{R1}{(R1+R2)}}{1 - \frac{R1}{(R1+R2)}} \right]. \quad (1)$$

This driving circuit is selected because of its simplicity, even though it cannot generate perfect sine wave. By changing R2 and R, a pseudo-sine wave can be generated and also frequency and magnitude of the output voltage are controllable.

III. ACS Fabrication

As discussed above, the microfluidic structure is assembled by a lamination process using multilayer epoxy-glass printed wiring board material. The fabrication sequence is shown in Fig. 3. The starting material consists of individual epoxy prepreg element layers. These layers are appropriately patterned using laser cutting. The layers are stacked together and are placed in a hot press for lamination. A temperature of 177 °C is maintained to ensure interlayer bonding. Fabrication samples with multiport distribution are shown in Fig. 7. Minimum fluidic channel sizes are 1000 μm in width and 300 μm in thickness.

In order to realize the goal of ACS development, this fluidic technology must be combined with the synthetic jet driver as described above. Fig. 8 presents an ACS device with silicon chip heater at its exit port. The heater array is designed to mimic heat generating components [e.g., line arrays of vertical-cavity surface emitting lasers (VCSELs)] [10]. The heater array has 100 platinum heater elements, each of which has a 75-μm pitch and a nominal 20 μm× 20 μm resistive heating area. Platinum works as the heater as well as the resistive thermal sensor, since the resistivity of platinum as a function of temperature shows extremely good linearity.

The ACS has a cavity with a diameter of 33 mm, a depth of 5 mm, a fluid passage with length of 10 mm, width of 10 mm, thickness of 1 mm, and a rectangular exit port of 10 mm ×

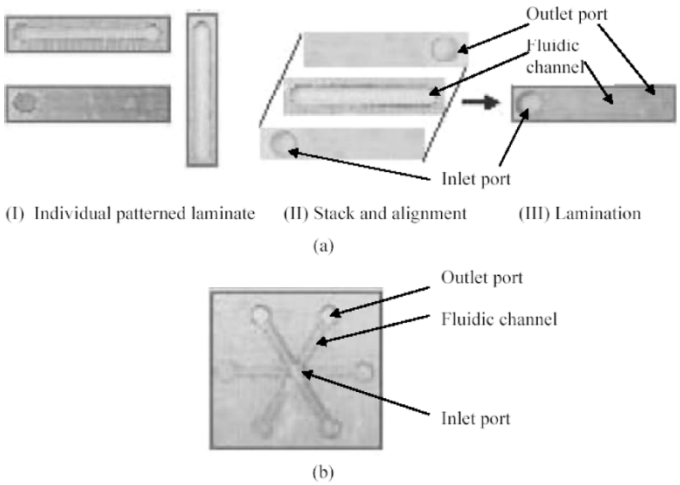

Fig. 7. Lamination process (a) fabrication sequence and (b) fabrication samples.

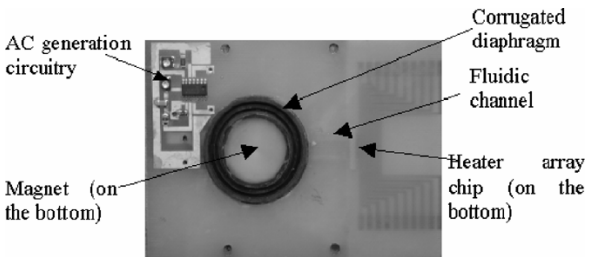

Fig. 8. Real ACS device with silicon heater.

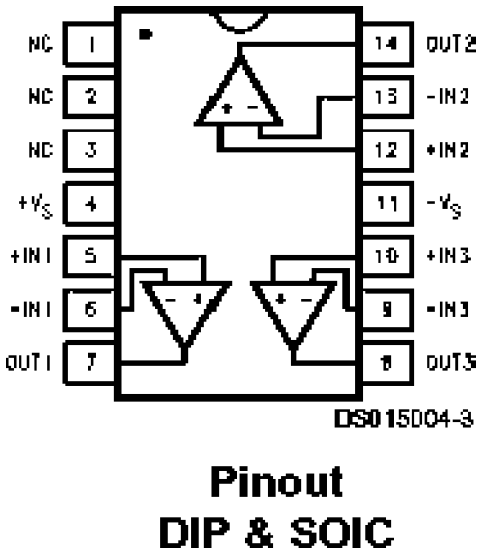

Fig. 9. Connection diagram of National Semiconductor CLC5623 chip.

1 mm. A coil is mounted on the prepreg center of the diaphragm. The coil leads are routed out through copper vias drilled in the PWB internal layers. The astable multivibrator driving circuit consists of active and passive components. Capacitors, resistors and potentiometers are individual packaged chips. The two op amps are in a commercialized National Semiconductor chipset-CLC5623. This is a triple, high output chip fabricated by an advanced complementary bipolar process. Its connection diagram is shown in Fig. 9. Only two of them are connected

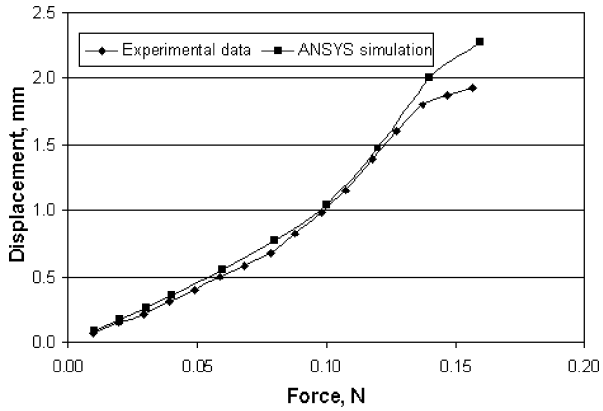

Fig. 10. Displacement versus static force.

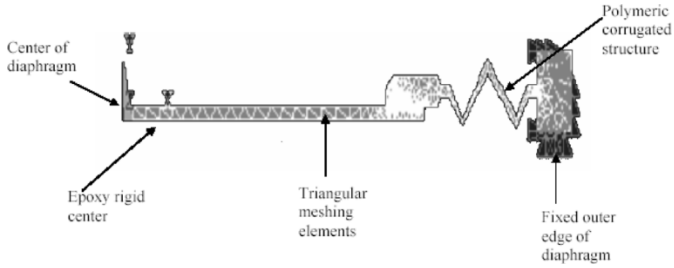

Fig. 11. ANSYS simulation model.

in the coil driving circuit. The highest output current can reach 130 mA. All components are surface mounted on the top surface of PWB with a copper interconnect pattern.

IV. Testing and Results

The deflection of the diaphragm is investigated in both static and dynamic modes. Static mode characterization was carried out using a displacement force test station (Model 921A by TRICOR System Inc.). In this test method, a force is applied on the diaphragm by a cylindrical tip with the diameter of 2 mm and the height of 5 mm, and the displacement is measured by the movement of the tip. The results are shown in Fig. 10. ANSYS simulation is also performed to provide a comparison with the experimental results. ANSYS is a finite element method (FEM) simulation tool. Due to the axis-symmetric structure of the diaphragm, a simplified two-dimensional model is applied to the simulation which demonstrates the cross-section cut plane of the diaphragm from the center to the outer edge as shown in Fig. 11. Triangular meshing elements are used to grid the entire structure. Two boundary conditions are applied: one is on the center edge which is free to move under certain forces; the other is on the outer edge of the diaphragm which is fixed without any freedom to move. Under this scenario, different forces are added upon the center of the diaphragm, and the deflections of the diaphragm are calculated by the FEM model. A comparison between the ANSYS simulations and the experimental results is shown in Fig. 10. As the applied force increases, the displacement increases as well. It is observed that the experimental results are in good agreement with the predictions from ANSYS modeling up to 0.1 N. Below 0.1 N, the diaphragm is operating in a linear regime. In actual use, the diaphragm is operated in

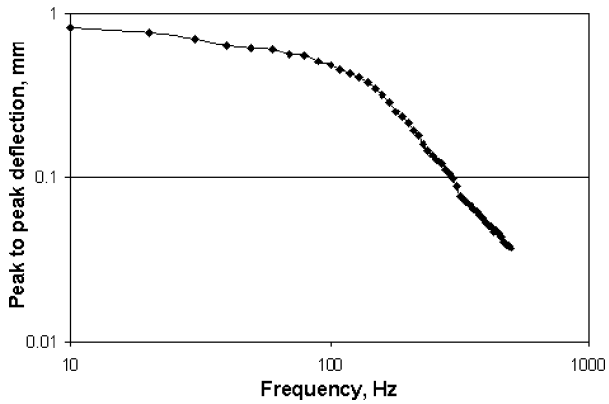

Fig. 12. Frequency response of the active cooling substrate device.

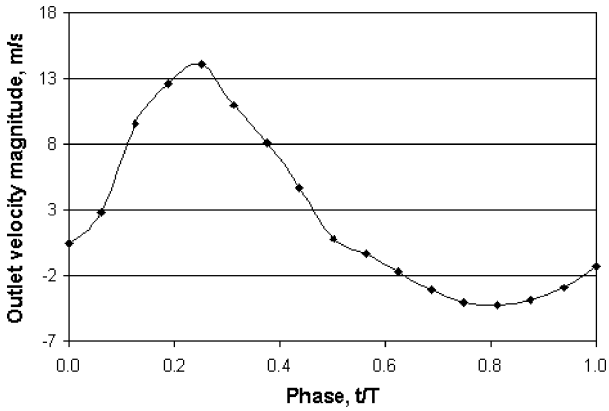

Fig. 13. Phase-averaged maximum velocity during one cycle of the actuator.

this linear regime (i.e., F $<$ 0.1 N); hence, ANSYS is satisfactory in this regime for design and optimize of the diaphragm in the linear regime under static mode.

When driven electromagnetically, the diaphragm operates in a dynamic mode. In this case, the frequency response can be studied to find the optimal operation frequency. A laser doppler vibrometer is used which is capable of measuring a moving displacement from a remote position using interferometry techniques. Fig. 12 shows the frequency response of the diaphragm vibration. The coil driving current is maintained constant at 70 mA RMS; thus, the electromagnetic driving force is kept constant and the consumed driving power is 0.06 W. Experimental data are plotted on a logarithmic scale. From the figure, the frequency of 100 Hz is selected to be the optimal operation frequency. At this frequency, the deflection is approximately 0.5 mm. Above this frequency, the deflection magnitudes decay at a slope of -40 dB/decade, indicating a second order over-damped system.

The synthetic jets generated by the ACS are studied experimentally by using hot-wire anemometry and particle image velocimetry. The jet output velocity magnitude is measured by hot-wire anemometry at a position 0.8 mm from the jet outlet. The microjet is operated at 100 Hz and at a coil driving current of 70 mA. Fig. 13 illustrates the phase-averaged maximum velocity in one cycle. At the full impingement position, the positive maximum velocity is about 14 m/s. At the full intake position, the negative maximum velocity is about 5 m/s. The time-averaged velocity is approximately 2.7 m/s. Along the

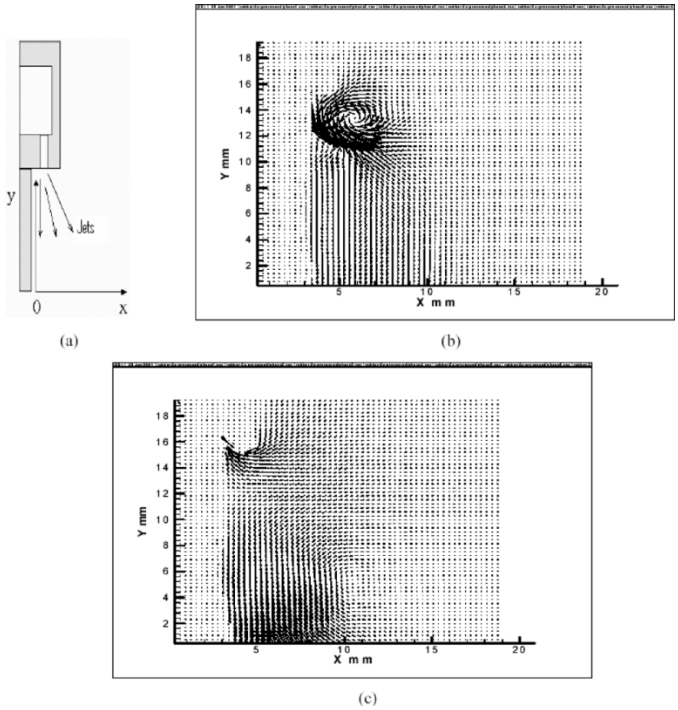

Fig. 14. Velocity field outside the channel exit. (a) PIV measurement setup. (b) PIV data at full impingement stroke. (c) PIV data at full intake stroke.

ACS centerline, the magnitude differences between these two maxima indicate locally there is a certain amount of air that is carried away from the channel exit. Therefore, it is desirable to have a larger difference between the two maxima which will result in greater net heat dissipation by the air jet.

Particle image velocimetry (PIV) is used to map the entire velocity field around the jet outlet. A sequence of PIV images of the velocity flow field at the jet outlet is taken phase-locked to the actuator driving signal at 18 equal time intervals. Fig. 14 shows the PIV images at full impingement stoke and full intake stoke within a cycle. Fig. 14(a) illustrates the PIV measurement setup. This two-dimensional image plane is the center symmetric plane of the active cooling substrate device. The jet exit is located at the upper left corner and the jet is blowing downward. Near the jet exit, the flow is dominated by the time-period formation and advection of a discrete vortex which ultimately undergoes transition to turbulence, slows down and loses its coherence. From Fig. 14(b) and (c), at the distance of 6–10 mm away from the channel exit (Y $= 10 - 6$ mm), there is a vortex development region during a half cycle from full impingement stroke to full intake stroke. The high momentum vortical structures generated during the impingement stroke have the ability to entrain the surrounding low momentum air into the jet cores. In addition, as the entrained fluid is continuously stretched and folded, localized instabilities are induced. All these features facilitate forced heat convection.

The cooling performance is tested in constant temperature mode. The heat-emitting source is a platinum film heating element array fabricated on a silicon chip. The ACS test bed exposes all the surfaces to ambient temperature (23 °C). The heater chip itself is calibrated to be a temperature sensor because of the linear relationship between its resistance and temperature. By monitoring the resistance across the element

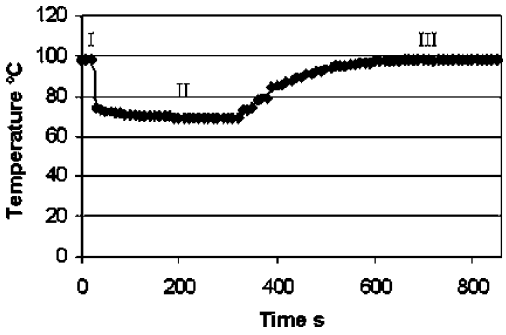

Fig. 15. Heat temperature changes in one cooling test cycle.

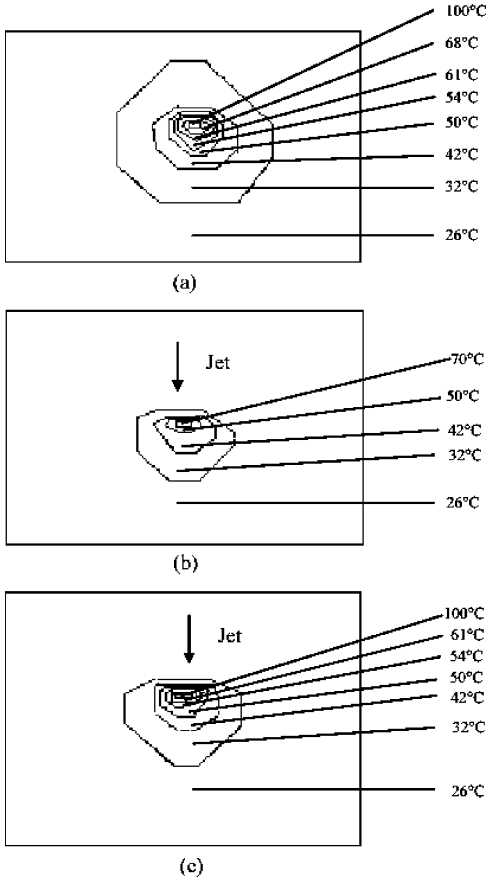

Fig. 16. Temperature distribution on PWB substrate in one cooling test cycle. (a) State I: without jet, heater at 100 °C. (b)State II: with jet, heater at 70 °C. (c) State III: with jet, heater at 100 °C.

on the chip, the heater temperature is obtained. The cooling performance measurement consists of three states as shown in Fig. 15, in which first the heater is heated to a steady temperature of 100 °C (state I). Then the jet is turned on until the temperature drops to its new steady-state value of approximately 70 °C (state II). The third step of the test involves increasing the power to the heater to reach the former steady temperature of 100 °C while the jet is operating (state III). The temperature distribution on the ACS during above three states is mapped by an infrared camera, as shown in Fig. 16. The high temperature region occurs directly above the heater which is located at 0.8 mm away from the jet exit. Temperature declines as the distance is further away from the center of the heater. The average temperature of each contour band is marked on the figure. At state I, the power input to the heater is 365 mW. The heat is dissipated from all the surfaces of the test bed by natural convection. At State III, the power input to the heater is increased to 707 mW to maintain the same heater temperature as state I. The increased power input to the heater array and the shrinkage of the hot temperature zone demonstrates that synthetic jets have a much higher forced convection heat transfer coefficient than the natural convection heat transfer coefficient at the downstream of the jet exit. Heat flux removal of 3.6 $\mathrm{W/cm^2}$ is achieved at a coil power consumption of approximately 60 mW. Errors of the cooling test are about 10% which are mainly due to the temperature measurement errors. Without surface enhancement (e.g., heat sinks), at temperature differences of up to 80 °C, traditional air forced convection achieves surface heat flux of 1 $\mathrm{W/cm^2}$ [11]. The ACS has comparable cooling performance to conventional fans, and performs better in some scenarios of interest, such as power consumption and PWB process compatibility.

V. Conclusion

In this research work, a MEMS ACS is implemented into multilayer printed wiring board based on synthetic jet technology. A fluoroelastomer is fabricated into corrugated structure to supply vibrating microfluidic momentum. This device is characterized from different perspectives including mechanical vibration, fluid mechanics and cooling performance. In many scenarios of interest, the integrated ACS has superior cooling performance compared with a traditional fan and has the potential for broad application in thermal management at the system packaging level. In addition to coupling with PWB substrates, it can also be combined with heat sinks or other packaging components to realize efficient active cooling.

Acknowledgment

The authors would like to thank Dr. A. Glezer and his Research Group at Georgia Tech for their assistance with experimental data collection.

References

[1] P. Gelsinger, "Microprocessors for the millennium: Challenges, opportunities, and new frontiers," in *Proc. 2001 IEEE Int. Solid-State Circuits Conf.*, Feb. 2001, pp. 22–25.
[2] D. Steinberg, *Cooling Techniques for Electronic Equipment*. New York: Wiley, 1991.
[3] R. Tummala, *Fundamentals of Microsystems Packaging*. New York: McGraw-Hill, 2001.
[4] B. Smith and A. Glezer, "The formation and revolution of synthetic jets," *Phys. Fluids*, vol. 10, pp. 2281–2297, Sep. 1998.
[5] O. Savas and D. Coles, "Coherence Measurements in synthetic turbulent boundary layers," *J. Fluid Mech.*, vol. 160, pp. 421–446, May 1985.
[6] M. Giovanni, *Flat and Corrugated Diaphragm Design Handbook*. New York: Marcel Dekker, 1982.
[7] Y. Wang, S. Bidstrup, G. Yuan, and M. Allen, "Printed-wiring-board microfluidics for thermal management of electronic systems," in *Proc. ECS'02 Int. Symp.*, May 2002, pp. 161–170.
[8] Y. Wang, G. Yuan, Y. Yoon, M. Allen, and S. Bidstrup, "A MEMS active cooling substrate for microelectronics thermal management," presented at the *Proc. ASME Int. Mechanical Engineering Congress R&D Expo*, Nov. 2003.
[9] A. Sedra and K. Smith, *Microelectronic Circuits*. New York, NY: Oxford Univ. Press, 1998.
[10] Y. Yoon and M. Allen, "Pt heater/sensor microarray for distributed fluidic cooling assessment," in *Proc. ASME IMECE/MEMS'01*, New York, NY, Nov. 2001.
[11] S. Kim and S. Lee, *Air Cooling Technology for Electronic Equipment*. Boca Raton, FL: CRC, 1996.

Yong Wang received the B.S. degree in chemical engineering and the B.S. degree in industrial engineering, and the M.S. degree in chemical engineering from Tianjin University, Tianjin, China, in 1997 and 1999, respectively, and the M.S. degree in electrical and computer engineering and the Ph.D. degree in chemical and biomolecular engineering from the Georgia Institute of Technology, Atlanta, in 2003.

He is currently a Development Associate at Praxair Technology Center, Tonawanda, NY. His research focuses on combustion process, heat transfer, and fluid mechanics.

Guang Yuan received the B.S.E. degree in mechanical engineering and the B.S.E degree in electrical engineering in 1995, and the M.A. and Ph.D. degrees in mechanical engineering from the Tsinghua University, China, in 1997 and 2000, respectively, all from Tsinghua University, Tsinghua, China.

She is currently a Postdoctoral Associate with the School of Electrical and Computer Engineering, Georgia Institute of Technology, Atlanta. Her research focuses on microactuator fabrication techniques.

Yong-Kyu Yoon (S'03) received the B.S. and M.S. degrees in electrical engineering from Seoul National University, Seoul, Korea, in 1992 and 1994, respectively, the M.S. degree in electrical and computer engineering from the New Jersey Institute of Technology, Newark, in 1999, and the Ph.D. degree in electrical and computer engineering from the Georgia Institute of Technology, Atlanta, in 2004.

His research focuses on developing RF passive components such as inductors, capacitors, and antennas, and developing three-dimensional microelectromechanical system fabrication techniques for RF and biological applications.

Mark G. Allen (M'89) received the B.A. degree in chemistry, the B.S.E. degree in chemical engineering, and the B.S.E. degree in electrical engineering, all from the University of Pennsylvania, Philadelphia, in 1984, and the M.S. and Ph.D. degrees from the Massachusetts Institute of Technology (MIT), Cambridge, in 1986 and 1989, respectively.

He joined the faculty of the Georgia Institute of Technology, Atlanta, following a Postdoctoral appointment with MIT. His research at MIT focused on micromachining techniques to create structures for the *in situ* measurement of mechanical properties and adhesion of thin films for use in microelectronic processing. He was also engaged in microsensors, microactuators, and in feedback-stabilized micromachined mirrors for laser applications.

Sue Ann Bidstrup received the S.B. degree from the Massachusetts Institute of Technology (MIT), Cambridge, and the Ph.D. degree in chemical engineering from the University of Minnesota, Minneapolis.

She is currently a Professor with the School of Chemical and Biomolecular Engineering, Georgia Institute of Technology (Georgia Tech), Atlanta. Prior to her appointment at Georgia Tech, she had spent two years as a Postdoctoral Associate with the Electrical Engineering Department, MIT. Her research interests intersect the areas of polymer engineering, microelectronic materials, and processing.

Dr. Bidstrup received the National Science Foundation Presidential Young Investigator Award, the DuPont Young Faculty Award, and the Georgia Tech Faculty Leadership Award. She is a Fellow of the Society of Plastic Engineers.